PAPER • **OPEN ACCESS**

Permanently magnetized elastomer rotating actuator using traveling waves

To cite this article: Jean-Baptiste Chossat and Herbert Shea 2024 *Smart Mater. Struct.* **33** 075028

OPEN ACCESS
IOP Publishing
Smart Materials and Structures
Smart Mater. Struct. **33** (2024) 075028 (12pp)
https://doi.org/10.1088/1361-665X/ad54ad

Permanently magnetized elastomer rotating actuator using traveling waves

Jean-Baptiste Chossat and Herbert Shea*

Soft Transducers Laboratory (LMTS), École Polytechnique Fédérale de Lausanne (EPFL), Neuchâtel 2002, Switzerland

E-mail: jean-baptiste.chossat@epfl.ch and herbert.shea@epfl.ch

Received 19 February 2024, revised 30 May 2024
Accepted for publication 5 June 2024
Published 24 June 2024

Abstract

We report a soft actuator that generates continuous rotation of an object placed on it by electromagnetically exciting circular travelling waves in a soft disk. The disk, that serves as the stator, is made of a stretchable composite consisting of segments of silicone elastomer in which hard ferromagnetic particles are embedded. Inspired by piezoelectric traveling wave rotary actuators, the disk's 16 sections are driven by underlying printed circuit board coils to create a flexural traveling wave on the disk's surface. The rotor can be any object directly placed on the stator: the traveling wave in the stator leads by friction to the rotation of the rotor. Unlike conventional electromagnetic motors that rely on a precisely controlled gap between stator and rotor, a concept incompatible with soft robotics, our device exploits the contact between rotor and stator and the associated dry friction to generate torque. Rotation speeds of over 6 rpm were obtained for a partially rice-filled balloon, 30 cm diameter, weighing 17 g. We report detailed speed and performance metrics when rotating plastic disks. With this rotating actuator, we demonstrate an innovative way to transmit torques and rotations within soft structures.

Supplementary material for this article is available online

Keywords: soft robotics, soft rotary actuator, traveling waves, magnetic elastomer

1. Introduction

The field of soft robotics has been the subject of growing academic interest in the past decade [1, 2]. However, soft robots' use in industrial applications remains very limited. Traditional robots, made using rigid materials, count hundreds of thousands of installations every year across various industries [3] while very few soft robots have found success outside of research laboratories. Thanks to their use of rigid frames and high torque rotating electromagnetic actuators, conventional robots boast high payload capacity and high actuation speed. In contrast, generating rotation using soft actuators remains largely an unsolved research question. Not only are soft rotating actuators performances underwhelming, but the proposed solutions often also rely on rigid components to transmit torque [4–6]. Yet given the central role of rotating actuators in traditional rigid robotics, soft rotating actuators can be expected to be enabling in the field of soft robotics.

In this paper, we report key elements of a soft rotating actuator based on a soft elastomer embedded with hard ferromagnetic particles and actuated using magnetic fields (B-fields). Rather than relying on rigid components such as gearboxes and shafts, our soft actuator is inspired by traveling wave piezoelectric actuators and relies on dry friction to transmit torque. In essence, flexural traveling waves are created and propagated on the actuator's soft surface. An object placed in contact with the actuator's surface is driven by the traveling waves, and spins, see figure 1.

* Author to whom any correspondence should be addressed.

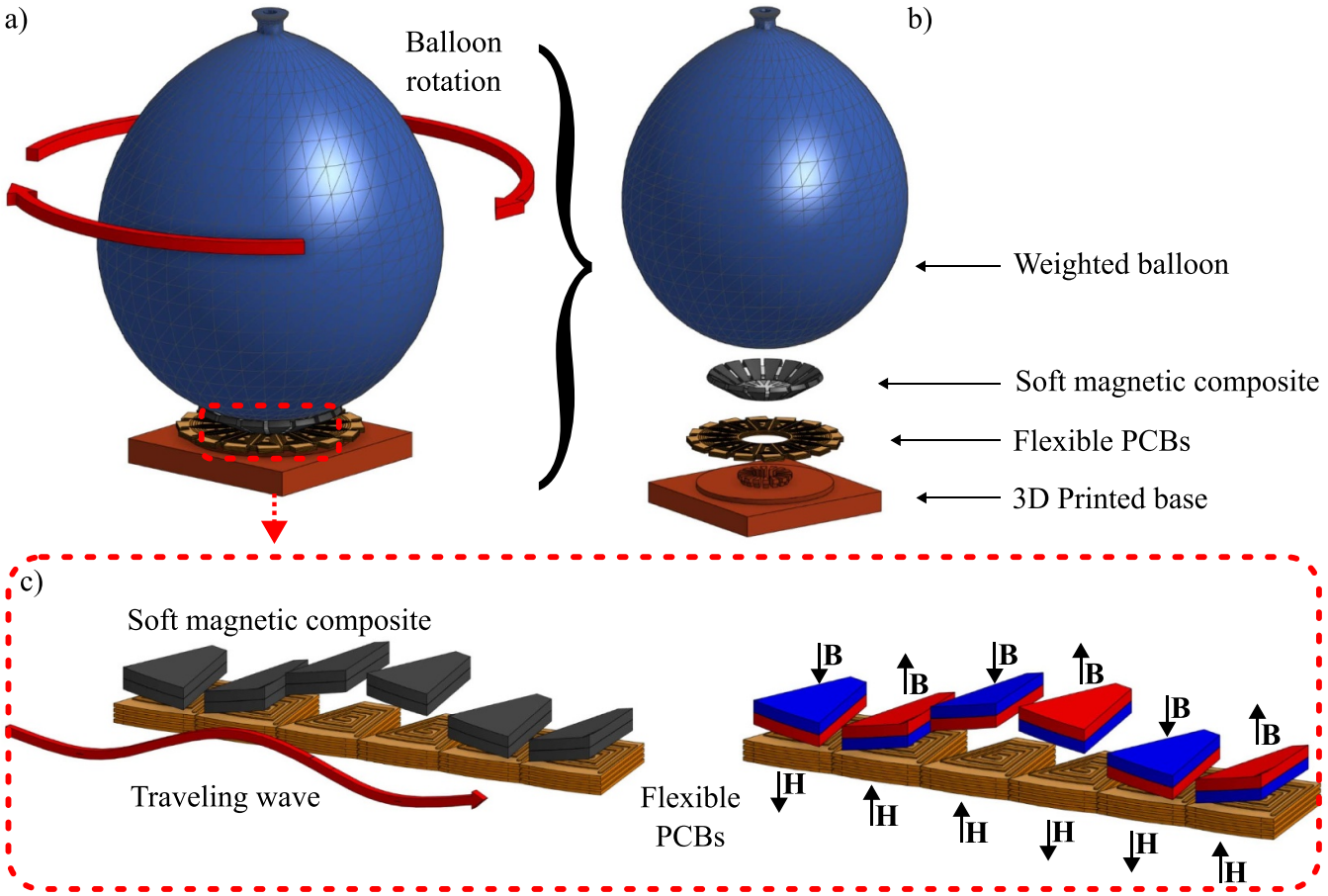

Figure 1. (a) Schematic of the actuator spinning a balloon (photo shown in figure 14), (b) exploded view showing the actuator's components, (c) 'unfolded' view of the soft magnetic composite disk and flexible PCB coils. Left: the traveling wave propagation. Right: applied magnetic field generated by the flexible PCBs, remanent magnetic field in the soft magnetic composite sections, and the resulting deformation of the soft layer.

1.1. Taking inspiration from traditional actuation

Brushless electromagnetic rotating motors are highly efficient [7]. However, these motors rely on a rigid and low friction bearings that must maintain the gap between stator and rotor even when the actuator is subjected significant loads. Maintaining such tight tolerances cannot be achieved in soft actuators.

Rotating piezoelectric actuators differ from rotating electro-magnetic actuators as, by design, the rotor and stator are in contact. These actuators rely on the deformation of piezoelectric elements (traveling wave) housed within the stator to drive rotor motion, exploiting the stator/rotor friction. Since piezoelectric actuators do not rely on a controlled gap between stator and rotor, the mechanism by which they create rotation is compatible with the use of soft materials. The most studied piezoelectric actuator is the traveling wave piezoelectric actuator [8]. Using traveling waves allow actuator rotation in both directions. There is always partial contact between rotor and stator, thus improving motion smoothness [8]. Such actuators rely on piezo-ceramics materials which are hard (Young's modulus on the order of several GPa), brittle, and are thus incompatible with soft robotics.

We report the design of a soft actuator inspired by traditional piezoelectric rotating traveling wave actuators. Designing such an actuator requires creating a resonant structure driven by fast (3–100 Hz) but soft actuators.

1.2. Soft materials for rotary actuation

Soft active materials such as liquid crystalline elastomers [9], shape memory alloys [10], shape memory polymers [11] or pre-strained polymer fibers [12] are all limited to low actuation speed (less than 3 Hz) due to their reliance on thermal stimulation. Chemically induced swelling due to the motion of ionic species such as ionic polymer-metal actuators suffer from even lower actuation speed [13]. Fluidic actuation widely used to drive soft robots. Pneumatic induced rotation [14] and torsion [15], as well as hydraulic bi-directional non-resonant traveling waves for locomotion ($\approx$2 mm s^{-1})

have been demonstrated [16]. Although frequently adopted, fluidic actuation usually relies on external cumbersome pumps and compressors.

Dielectric elastomer actuators (DEAs) are another widely-used soft active materials. DEAs are characterized by their high energy density and large actuation bandwidth. However, rotating actuators based on DEAs typically rely on gearboxes, shafts, and hard frames to decouple torque generation from active element [4, 5, 17–19].

A number of soft electromagnetic actuators has also been proposed. Some rely on miniature rigid components [20] while others use soft analogues to wires such as liquid metal channels [21]. However, liquid metals such as eutectic Gallium Indium (eGaIn) have a significantly higher resistivity than copper ($\rho_{\text{copper}} \approx 1.68.10^{-8}\ \Omega\ \cdot\ \text{m}$; $\rho_{\text{eGaIn}} \approx 2.94.10^{-7}\ \Omega\ \cdot\ \text{m}$) [22].

Composites of soft elastomers and a powder of hard ferromagnetic particles can also be used instead of conventional magnets [23–26]. Such silicone elastomer composites simultaneously exhibit hard ferromagnetic and soft mechanical properties. We shall refer to this class of materials as soft magnetic composite in this paper. Soft magnetic elastomer composites have recently been investigated in various publications such as soft medical robots [27], micro-robots locomotion [28], and peristaltic pumping [29]. They offer simple control [26] and rapid actuation (up to 140 Hz) [23, 25, 30]. Indeed, compared with traditional magnets embedded in soft elastomers, micron-sized ferromagnetic particles have a higher surface to volume ratio, which makes them less likely to rotate or to break free from the soft elastomer matrix. Small particles also allow the composite to deform continuously rather than piecewise. A recently published soft rotating electromagnetic actuators made from soft wires and soft magnetic composites required rigid components to ensure torque transmission [6].

The characteristics of soft magnetic composites make these materials promising candidates for creating soft resonant structures. In this paper we apply key elements of the piezoelectric traveling wave actuator theory to drive a soft magnetic composite using time-varying magnetic fields. Stacked flexible printed circuit boards (flex PCBs) are used to create local magnetic field gradients that we can rapidly modulate. The magnetic field gradients move the sections of the stator made with the soft magnetic composite, generating a circular traveling wave. The friction between the actuator and the object placed on it results in the object's rotation, see figure 1. We report here the first demonstration of a soft bi-directional and continuously rotating actuator operating with traveling waves, and also the first demonstration of using soft magnetic composites as a means to generate traveling waves.

2. Actuator operating principle

The actuator presented in this paper relies on flexural circular traveling waves to transmit torque from the actuator (the stator) to the load (the rotor). The flexural traveling waves generate an elliptical retrograde trajectory for points at the actuator's surface, see figure 2. Since the trajectory is closed, there is no overall motion of the stator. However, the actuator and the load are in contact at the ellipse's apex, where the stator pushes on the rotor. As a consequence, a net motion is transmitted from the actuator to the load as illustrated in figure 3.

2.1. Generating travelling waves

Traveling waves are commonly generated in piezo-electric actuators by assembling several piezo-transducers into a ring. The traveling wave is created by driving the piezo-transducers to create two out of plane flexural standing waves of the same frequency, the combination of which is a traveling wave whose motion depends on the phase difference between the two stading waves. The standing waves frequency is determined by the stator dimensions and by the materials used. The actuator operates at resonance to maximize amplitude. To create two standing waves with the same frequency but with distinct phase, the ring is divided into several parts, two of which are driven. Both driven parts are actuated with a sinusoidal signal, but with a phase shift, shown in figure 4. This is shown in equation (1) in which the traveling wave is the superposition of two standing waves. N is the mode number, ω the angular frequency, λ the wavelength and A the peak wave amplitude [31, 32],

$$\begin{aligned} u_t(\theta,t) &= A\left[\cos(n\theta)\cos(\omega t) + \cos\left(n\theta+\frac{\pi}{2}\right)\cos\left(\omega t+\frac{\pi}{2}\right)\right] \\ u_t(\theta,t) &= A\cos(n\theta-\omega t)\,. \end{aligned} \tag{1}$$

To generate a traveling wave, the two standing waves must be created independently. The magnetic composite layer is separated into four sections: two of them being driven to create standing waves, and two non-driven sections separating the driven sections. The length of these non-driven sections must be equal to odd multiples of the quarter wavelength. For example, one section's length could be $3\lambda/4$ while the other would be $\lambda/4$ as shown in figure 2.

The actuator's operating resonant frequency depends on the speed of flexural waves in the stator's material, on the ring's perimeter length, and the targeted resonant mode. When a steady state is reached, it is well established [32–34] that points at the stator's surface describe an elliptical retrograde motion, represented in a profile view in figure 3 and equation (2). It is this motion, coupled with friction between stator and rotor, that drives the actuator load's rotation. A point at the stator's surface following an ellipse is described by the following parametric equations [34]:

$$\begin{aligned} x(t) &= A_x\cos(\omega t) \\ y(t) &= A_y\sin(\omega t) \end{aligned} \tag{2}$$

in which x, y, A_x, and A_y respectively represent the ellipse's horizontal motion, vertical motion, horizontal displacement amplitude, and vertical displacement amplitude,

$$v_h = \frac{\mathrm{d}x}{\mathrm{d}t} = -A_x\omega\sin(\omega t)\,. \tag{3}$$

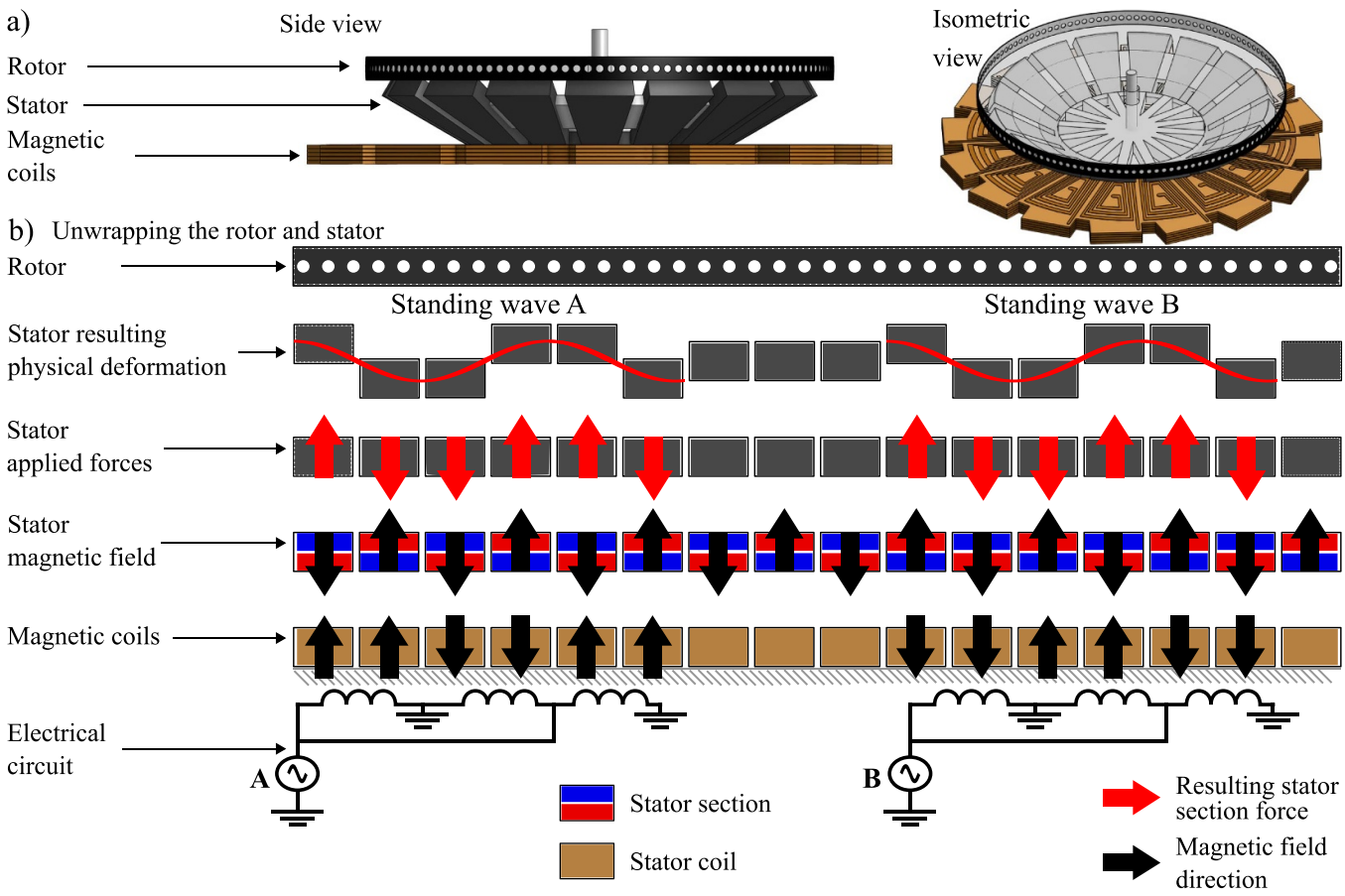

Figure 2. (a) Schematic representation of the overall stator and rotor assembly. The PMMA plate used for characterisation in section 4 is used as a rotor example here. (b) Both stator and rotating flat disk are unwrapped. The electrical drive circuit, flex PCB coils, soft magnets, magnetic fields, and associated deformations of the soft magnetic composite layer are shown, along the stator.

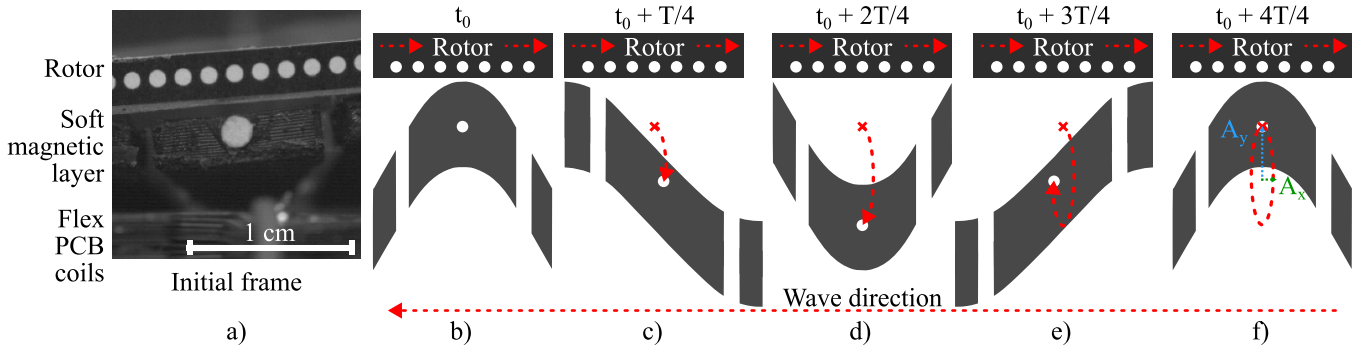

Figure 3. Idealized soft magnetic composite deformation due to a right-left traveling wave. Red dotted arrows represent various parts in motion. A frame of the device as captured by the high speed camera is shown in (a). The white dot on the stator's surface describes an elliptical trajectory. The impact of the traveling wave is described from (b) to (f) by quarter periods increments.

Assuming no slip, $v_h = \mathrm{d}x/\mathrm{d}t$ is the horizontal velocity, as such expected maximum absolute rotation velocity is attained at $\omega t = -\pi/2 \mod \pi$.

2.2. *Traveling waves in a soft magnetic composite actuator*

Although our actuator design is inspired from traditional traveling wave piezo-electric rotating actuators, there are major design differences. First, the materials used for the stator's upper part are about 4 orders of magnitude softer than their traditional counterparts ($E_{\mathrm{PZT}} \approx 64$ GPa ; $E_{\mathrm{Composite}} \approx 1.76$ MPa). Second, piezo-electric transducers rely on electric fields applied between surface electrodes, while electromagnetic actuation allows operation with the soft magnetic composite layer both curved and not in contact with the coils. Third, the use of soft materials means that, for a given resonant mode, the driving frequency used will be significantly lower than in a traditional piezoelectric actuator.

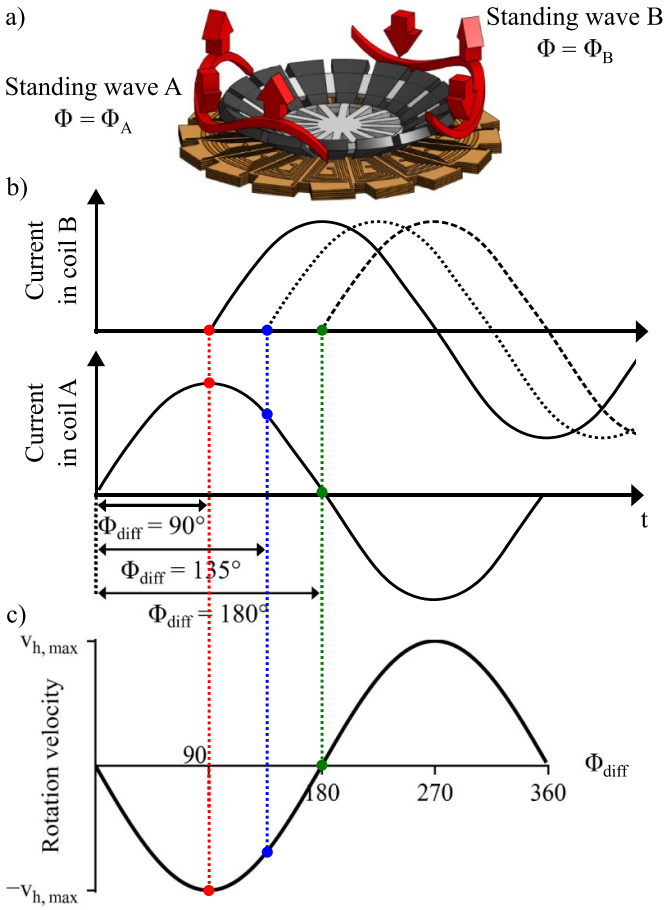

Figure 4. (a) The traveling wave is generated due to the interaction of the standing waves 'A' and 'B'. (b) The standing waves' phase difference. (c) The rotor horizontal velocity depends on the phase difference.

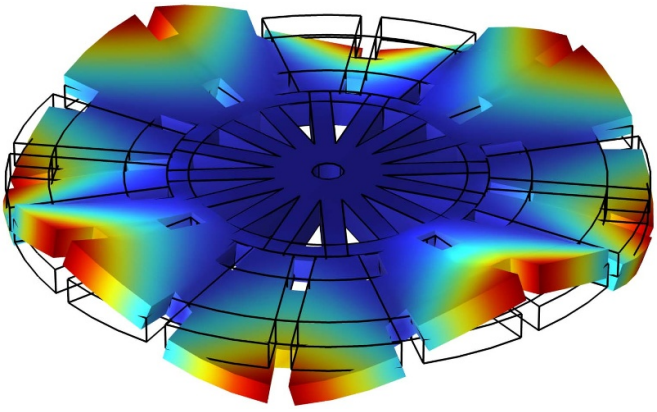

Figure 5. Finite element modeling (COMSOL, Multiphysics, Solid Mechanics module): eigenfrequency simulation. This figure illustrates the 8th mode flexural wave. See supplementary data figure 7 for more information.

3. Actuator design

As shown in figure 1, the actuator is composed of three elements: *i)* a base made of 3D printed polyethylene terephthalate glycol (PETG), *ii)* a stack of nine flex PCBs and *iii)* the soft magnetic composite layer. The flex PCBs are stacked to create 16 individually addressable flat electromagnetic coils. Similarly, the soft magnetic composite layer consists of 16 magnetic sections linked by a soft non-ferromagnetic polymer.

We choose to divide the soft magnetic composite layer into 16 equal sections as a trade-off between competing parameters with the goal of maximizing rotating performance. First, the volume of soft magnetic composite decreases with higher number of sections due to the increase of non-magnetic elastomer used to mechanically link the sections. This favors lower section count. Second, as explained in section 2, a number of sections in the soft magnetic composite layer must not be driven. The length of the non-driven section is a multiple of $\frac{\lambda}{4}$, the resonant frequency wavelength. Since higher resonant frequencies lead to smaller wavelength, using higher resonant modes allow to minimize the non-driven soft magnetic composite sections. Creating higher frequency resonant modes requires a higher number of sections to control. Third, the soft magnetic composite must also sustain at least three complete flexural waves as it ensures load stability by providing it with three contact points at any time [33]. Therefore, we chose to divide the soft magnetic composite layer into 16 sections. As shown in figures 2 and 5, this results in the soft magnetic composite layer being able to sustain a traveling wave that is four wavelength long.

Both the flex PCBs and the soft magnetic composite layer have an external diameter of 60 mm. The flex PCBs are mounted on the base with double-sided polyimide tape, while the soft magnetic composite layer is placed on top of the flex PCBs. The soft magnetic composite layer is kept aligned with the flex PCB coils thanks to the base. When placed on the base, the soft magnetic composite layer is subjected to a small radial stress, which leads to the magnetic composite layer slight upward curve, away from the base (see figure 1).

3.1. Soft magnetic composite layer design

The soft magnetic composite layer is 2.5 mm thick, weighs 16.6 g and is composed of 16 soft magnetic composite sections of 15 mm radial length (see figure 6(a). Each soft magnetic composite section is vertically aligned with a flex PCB electromagnetic coil of similar area. Creating traveling waves requires dividing the soft magnetic composite layer into two regions separated by regions in which no deformation is imposed. By not energizing the coils beneath a number of soft magnetic composite sections we can create these gap regions. Since we do not modify the soft magnetic composite layer, wave propagation is unaffected. We designed the gaps to be equal to $\lambda/4$ and $3\lambda/4$ arc lengths. We elected to use 1 and 3 inactive electromagnetic coils to create the gap regions (see figure 4). The 16 soft magnetic composite sections are linked to each other to alternate in magnetization direction. This was done to focus the magnetic field gradient close to the actuator, and therefore maximize the impact of the close-by flex PCB coils.

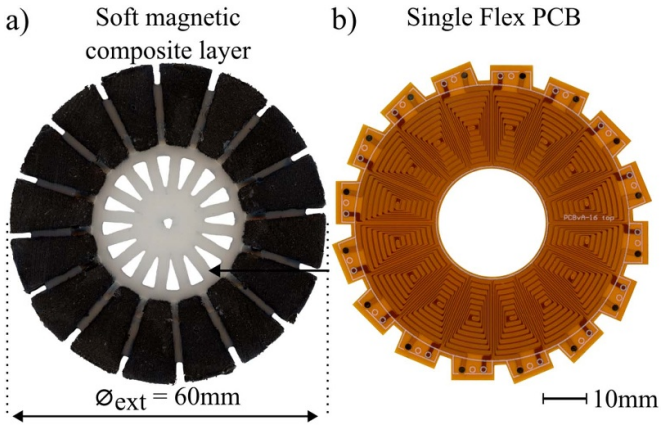

Figure 6. Top view of (a) the soft magnetic composite layer and (b) a single layer flexible PCB.

3.2. Soft magnetic composite manufacture

The soft magnetic composite is prepared by mixing a silicone elastomer (Dragon skin 10NV, Smooth-On) with high coercivity ferromagnetic particles (MQA-39-15-80 M, Magnequench) using a planetary mixer (Thinky Are-250) for 30 s at 2000 rpm. The particles were chosen for their strong remanence ($B_r = 1.317$ T), and the elastomer selected for its softness and relative low viscosity. Zhao *et al* [26, 27] had maximized the energy density of soft composites following:

$$W \propto \frac{M^2 H^2}{G} \quad \text{where} \quad G = G_0 \exp\left(\frac{2.5V}{1 - 1.35V}\right) \tag{4}$$

where W denotes the work produced by a soft magnetic composite section under a uniform magnetic field, producing a force F and deformed by δ from its original position, such as $W = \delta F$ [27]. M is the composite magnetization, H the applied magnetic field, G the composite shear modulus using the Mooney model, and V the particle volume loading. Although this model assumes spherical particles, it is a good approximation that allows maximizing a section's work according to particles loading. Following this model, the optimal particle fraction by volume is close to 30%. This set of equation can be understood intuitively as representing the actuator trade-off between strong magnetization and low shear modulus due to high particle loading. Assuming an incompressible composite material ($3G \approx E$), and using the reported base elastomer Young's modulus ($E_{\text{DS10NV}} = 0.5$ MPa [35]), we can estimate the soft magnetic composite Young's modulus such as $E_{\text{Composite}} \approx 1.76$ MPa [27].

3.3. Soft magnetic composite layer assembly

Several groups have described how to manufacture soft magnetic composite samples with continuously varying magnetization. The most common method is to apply a strong unidirectional magnetic field on a bent or folded sample [36]. Although a folding approach can yield a multi-polar soft magnetic composite layer using a continuous soft magnetic composite sample, we found that given the required number of folds such an approach led to magnetic poles of uneven boundary and subjected the soft magnetic composite sample to high mechanical stresses prior and during magnetization. Instead, we decided to assemble and combine several separate soft magnetic composite sections into a single composite structure such as in [29]. To do so, the soft magnetic composite composite was first poured and compression molded into 16 separate 2.5 mm thick sections. The sections are designed based on a single ring with internal and external radii respectively of 15 and 30 mm, and that is divided into 16 equal sections separated by 2 mm gaps. Once filled, the molds were secured for 24 h between large N45 NdFeB permanent magnets (S-70-35-N, Supermagnete) held by aluminum framing and creating a pseudo-uniform magnetic field of at least 200 mT (see supplementary figure 4). This procedure led to an increase in magnetic remanence of about 42.2% compared with non-exposed soft magnetic composite sections (see supplementary figure 1 and table 1). This has been shown to be due to the hard ferromagnetic filler moving into column-like structures aligned with strong magnetic fields prior to the elastomer curing [37, 38]. The locked molds were then placed in an impulse magnetizer (IM-K-010 020-A, Magnet-Physik) and exposed to 3 pulses of 2000 kA m^{-1}. Finally, in order to assemble the 16 separate sections into a single soft moving ring, the sections

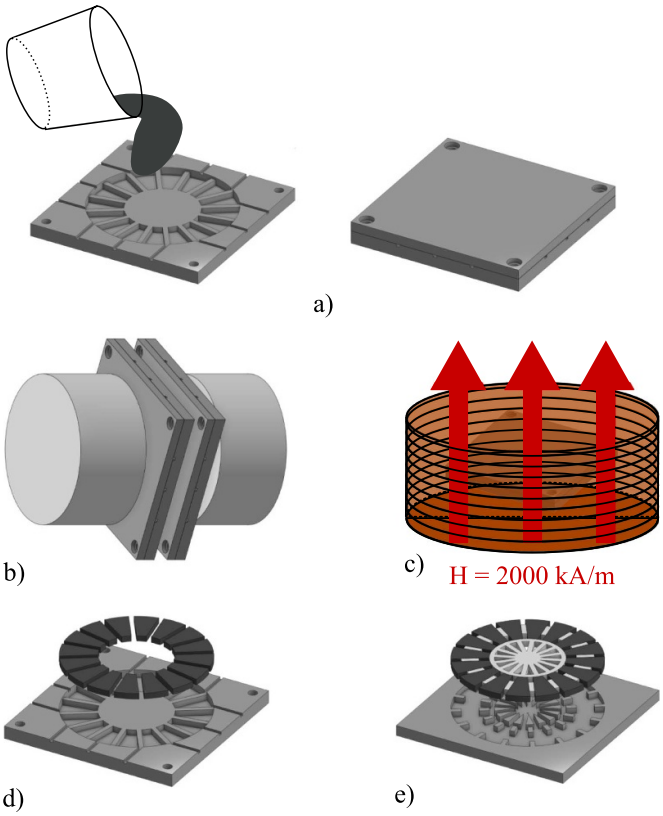

Figure 7. Manufacturing process. (a) Composite compression molding, (b) composite curing between magnets, (c) pulse magnetization, (d) unmolding of the separate sections, (e) molding and joining the sections together.

were placed in a new 3D printed mold (MK3S+, Prusa) and the same base elastomer (Dragon Skin 10 NV, Smooth On) was poured and fills the gaps according to the design detailed in section 3.1. We found this manufacturing approach, detailed in figure 7, beneficial in several ways. First, it led to high manufacturing yields. Second, we observed high repeatability in the sections' measured magnetic field. Third, this method can scale up as long as individual soft magnetic composite sections are large enough to be manipulated.

4. Experimental results

4.1. Setup description

We used a digital oscilloscope and frequency generator (Analog discovery pro 3450, Digilent) both to generate the command signals and to measure the electromagnetic coils' voltage. The command signals were sent to two power amplifiers (DC453B-B, Analog Devices) operating in non-inverting mode with a gain of 2 (see supplementary figure 2). The power amplifiers are supplied using a ± 18 V, 5 A power supply (Agilent Technologies N6700B, equipped with two N6751A modules). The soft rotor deformations are recorded using a high speed camera (VEO-E 310 L, Phantom) equipped with a 20 mm focal length spacer and a 55 mm telecentric lens (TEC-55, Computar), as shown in figure 8. The camera is operated at 4000 frames per seconds and using a 256×256 pixels frame (figure 9 and SI video). The flex PCBs are 200 μm thick double sided and with 55 μm thick copper traces. A single coil made using a stack of 9 flex PCBs has a resistance $R_{\text{coilstack}} \approx 5.51\,\Omega$, with an average single double sided coil resistance $R_{\text{coil}} \approx 0.61\,\Omega$ for a total of 108 turns. Each coil stack is wired in series with an adjacent coil stack, and all coil stacks for a single phase are wired in parallel. Accounting for the resistance of all the coils for a single phase as well as the connections to the power amplifiers $R_{\text{phase}} \approx 5.5\,\Omega$. Three different flex PCBs were designed, allowing each of them to be stacked and soldered, reducing the need for wires and allowing some degree of modularity when building the electromagnetic coils (see supplementary figure 5). Each flex PCB soldered weighs about 1.75 g, yielding a total of about 15.75 g for a stack of nine flex PCBs as used in our setup.

4.2. Characterizing the actuator

To measure the actuator characteristics we cut polymethylmethacrylate (PMMA) plates of various thicknesses into disks. Using rigid disks allowed us to ensure even weight distribution during rotation as well as consistent contact dynamics with the stator across samples. The disks were cut using a CO2 laser (Speedy 300, Trotec) with an external diameter of 60 mm to match the stator's, and with a center hole of 3 mm. The disks' edges were marked with white-on-black 1 mm diameter circular markers to optically track the disks position during operation. The disks were placed on top of the soft magnetic composite layer and constrained by a smooth axle going through the disk's center.

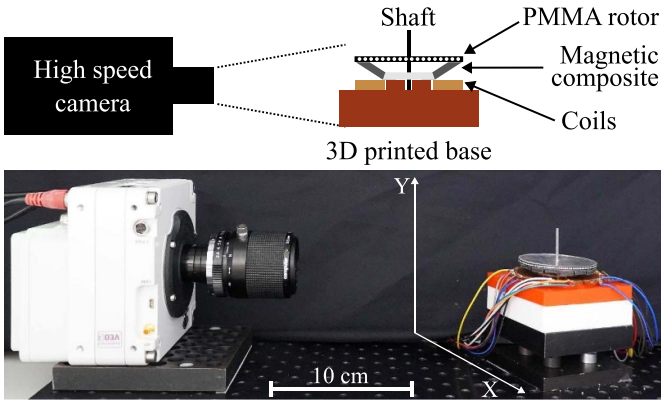

Figure 8. Schematic drawing and photo of the experimental setup, side view.

4.2.1. Rotation speed. We study the impact of the standing waves' phase difference on the rotation speed using the aforementioned rigid PMMA rotors. The goal of this experiment was twofold: *i)* find and measure the maximum experimental rotation velocity and *ii)*, determine how the rotation velocity as a function of phase corresponds with the model of a traveling wave actuator. To do so, PMMA rotors of various thicknesses were placed on top of the soft magnetic composite rotor (see figure 11). A Python script is used to control the signal generator, start a high speed camera recording, capture the electromagnetic coils' voltage and change the phase difference between the two standing wave driving signals. The driving signals from the signal generator were set at 70 Hz and 2.5 V of amplitude. The resonant frequency was determined experimentally.

The driving signals supply the electromagnetic coils for one second, while the rotor and stator positions are captured for about 1.2 s using the high speed camera at 4000 frames per second. After each movie, the phase difference is increased by a 10° step. The experiment is run five times for each PMMA rotor. The rotor displacement is later computed with a Python script comparing the location of the six innermost rotor markers in consecutive frames, and then averaging to a single rotor displacement. Knowing the rotor markers' position in each video frame, marker size, and camera frame rate we obtain the rotor's change in position for each frame (i.e. the instantaneous velocity). The cumulative sum of the rotor position changes for each frame yields the rotor's displacement over time (see figure 10). As this data is reasonably linear, it can be fitted with a straight line, the slope of which is the rotor average velocity. The average velocity and average velocity standard deviation are then calculated by comparing each of the five data series for each PMMA rotor.

Using this method, the average rotation velocity can be measured in various conditions. The weight of the rotor can be changed, as well as the phase difference between the two standing waves. Although varying the standing waves phase difference has little practical use, it is nevertheless very helpful to verify the actuator behavior as we can compare expected (figure 4) to measured rotor rotation velocity as a function

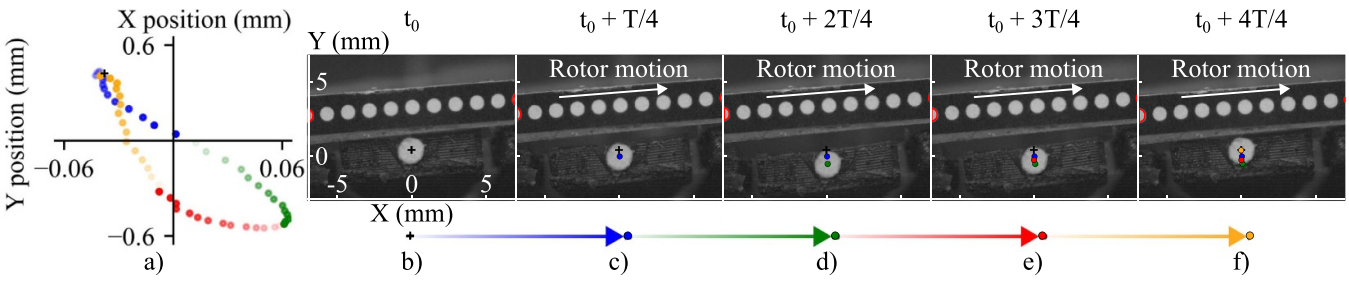

Figure 9. (a) Measurement of the marker position on the soft magnetic composite stator (not the dots on the rotor) during a full period during the actuator operation at 70 Hz, 120° phase difference, and with the 3 mm thick PMMA rotor, starting at $t_0 = 0.496\,25$ s. (b)–(f) High speed images corresponding to quarter period intervals. In frame (a) each quarter period interval corresponds to a single color and the point's transparency increase linearly within the time interval. The pictures are tagged with the stator marker consecutive positions, reflecting the graph (a) markers. The rotor outer markers are highlighted in red to emphasize the rotor motion.

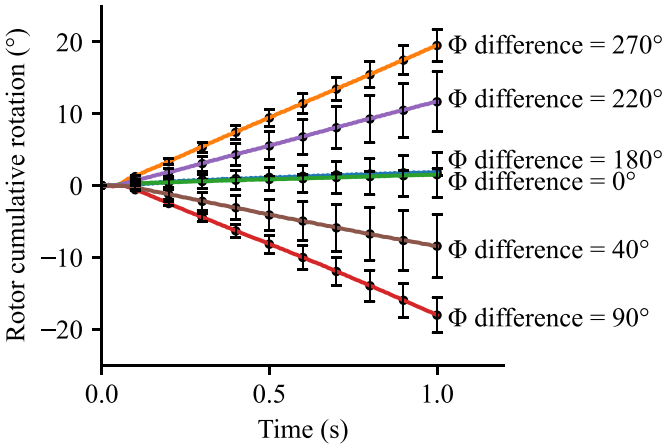

Figure 10. Cumulative rotating of 3 mm PMMA rotor in degrees during one second of actuation. The cumulative rotation depends on the driving signals' phase difference and is presented at key (0°, 90°, 180° and 270°) and intermediary (40° and 220°) values. The driving signal frequency is 70 Hz. The data has been averaged over five experiments. Error bars represent one standard deviation.

of standing waves' phase difference (figure 11). Varying the rotor's mass is important to measure the actuator response to objects of various masses.

When loaded with 2, 3, and 4 mm thick PMMA rotors, the rotation velocity continuously varies with the driving signal phase difference. From close to 0 rotation per minute (rpm) at 0° and 180° , the rotation velocity reaches maxima close the predicted values of 90° and 270° . This pseudo-sinusoidal behavior is well in line with expectations from the no-slip average rotation velocity presented in equation (3) and figure 4. The small standard deviation and smoothness of the graphs in figure 11 indicate good actuation repeatability and control. Slight variations are probably due to differences in resistance between the coils due to electrical connections. As expected, the lighter 2 mm thick PMMA rotor reaches the highest average rotation velocity. However, the 4 mm thick PMMA plate reaches a higher average rotation velocity than the 3 mm thick plate. We think this is due to a change in contact dynamics and improved magnetic response as the soft magnetic composite layer is closer to the electromagnetic coils. Performance degrades significantly with higher thickness plates. When using 5 mm and 6 mm thick PMMA plates, not only does the maximum average rotation velocity decrease and the standard deviation increase, but also the rotation control is impaired with nearly no observed clockwise rotation for the 6 mm thick plate. We suspect that this is due to the curved soft magnetic composite layer collapsing under the PMMA rotor weight, touching both the electromagnetic coils and the rotor, and thus changing in resonance frequency.

4.2.2. Torque, mechanical power & efficiency. Using rigid PMMA rotors and measuring their rotations allows us to estimate the torque produced by the actuator. To do so, we use I, the rotor's moment of inertia, a the rotor's angular acceleration and τ the rotor's experienced torque: $\tau = I.a$ (see figure 12). For a given dataset, we select the data series for which the overall clockwise and counterclockwise velocity was highest. A Savitzky-Golay filter (15 points, 3rd order polynomial) is applied on the data series' instantaneous velocity prior to deriving to get the acceleration. The torque data series is then computed following the above mentioned relationship. In theory, after the stator resonance is established, continuous stator-rotor contact produces constant torque. However, in real conditions the stator-rotor contact varies, leading to acceleration and deceleration within the actuator's resonant time period (1/70 Hz). Consequently, to estimate the actuator's torque we used the average of the rotor's torque envelope (see supplementary figure 6). By using PMMA plates of various weights, we measured the actuator's angular velocity ω and torque τ as a function of the normal force applied on the stator, as shown in figure 12. The maximum rotation velocity and torque are obtained by averaging the maximum clockwise and counterclockwise results of all five series of phase difference sweep experiment, for each of the different PMMA rotor. As expected, and excluding the heaviest load (m5), there is an inverse trend between actuator's torque and rotation velocity as the rotor mass increases.

The mechanical power and efficiency can also be estimated from the same data series using $P_{\text{mech}} = \tau.\omega$ and for the efficiency $\nu = P_{\text{mech}}/P_{\text{in}}$. P_{in} is the electrical power used by

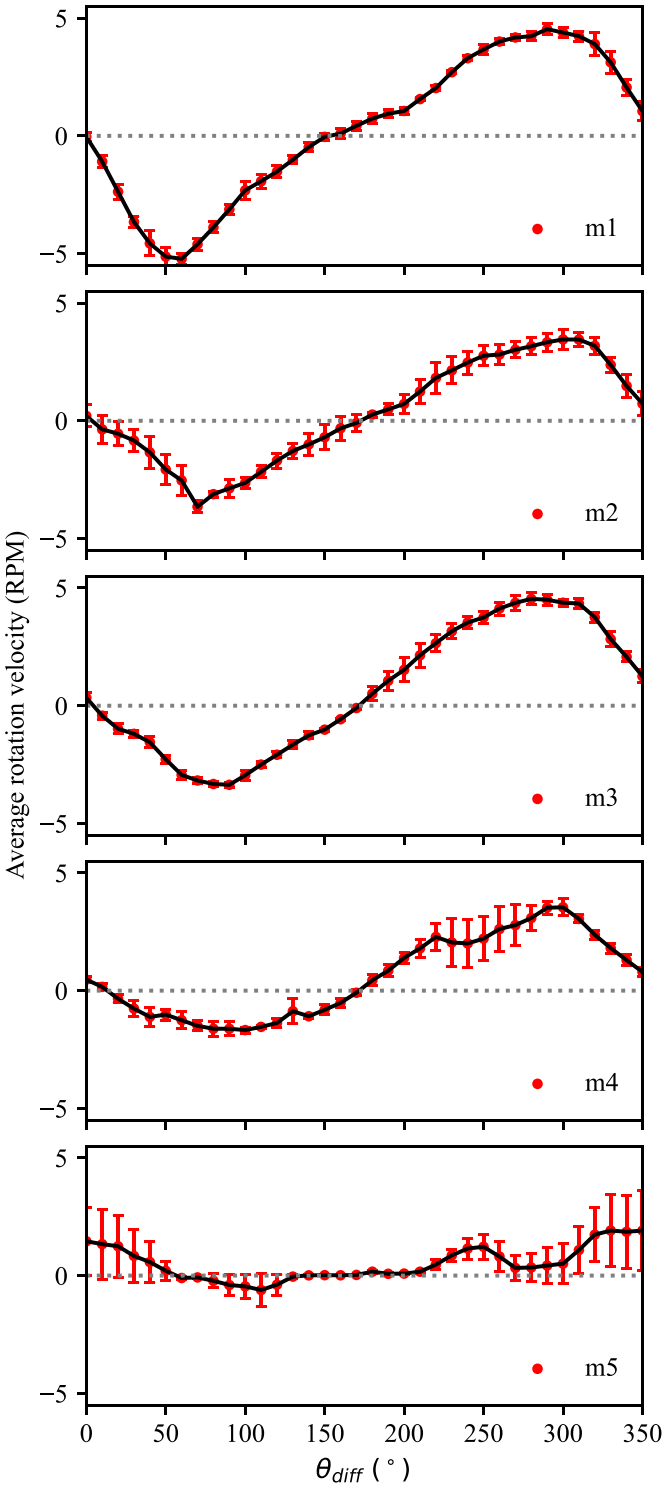

Figure 11. The average rotation velocity in rpm for various PMMA rotors as a function of the driving signals phase difference. The rotors m1, m2, m3, m4 and m5 respectively weigh 7.51 g (2 mm thickness), 10.14 g (3 mm thickness), 12.17 g (4 mm thickness), 17.60 g (5 mm thickness), 19.00 g (6 mm thickness). Error bars indicate a standard deviation, and the dashed grey line corresponds to the expected sinusoidal rotation velocity for a given PMMA rotor measured maximum rotation velocity.

the actuator and calculated as follows $P_{\text{in}} = V_{\text{rms}}^2/R_{\text{coil}}$. The mean actuator mechanical power and efficiency are presented in figure 13. The results are in line with expectations and results from figure 12. Since input power is not varied, overall actuator efficiency is maximum at for medium loads.

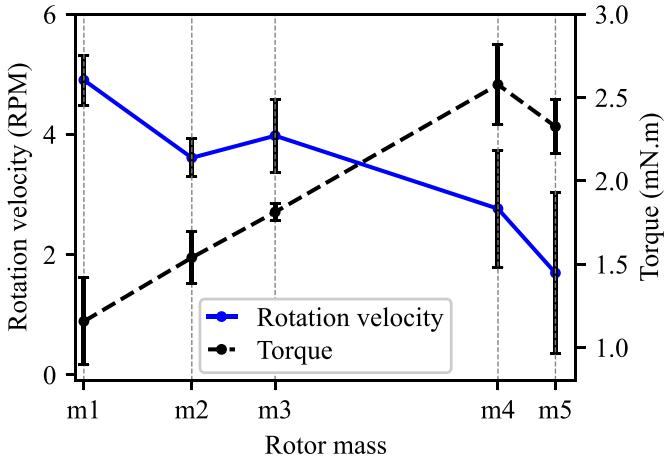

Figure 12. Peak rotation velocity and torque as a function of rotor mass.

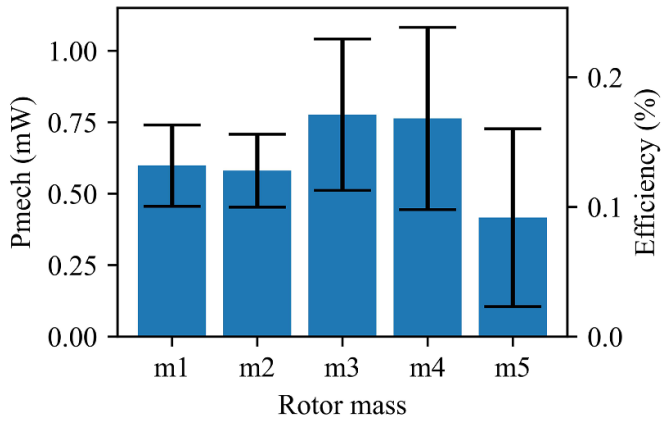

Figure 13. Actuator mean and standard deviation mechanical power and efficiency as a function of the PMMA rotor mass.

4.3. Rotating a soft load

An inflatable rubber balloon was used as a demonstration of the actuator capabilities. We used a balloon as they are indisputably soft, can stretch to various diameters and can be weighed down using different non-ferromagnetic fillers. We inflated our balloon to reach a maximum diameter of 61 cm, and added 15.2 g of rice (total balloon mass: 17 g). Adding rice was helpful to increase the balloon's mass as well as lower it is center of mass, thus ensuring the balloon does not fly away and stays centered on the soft magnetic composite stator. As can be seen in the SI movie, the balloon rotation velocity averaged at 3.5 and 6.2 rpm respectively for when using driving signals 90° and 270° out of phase. The actuator performance with a balloon are comparable but superior to the performance reached with the m4 labeled PMMA rotor (see figure 11). This is likely due to the increased stator/balloon contact surface and contact surface friction.

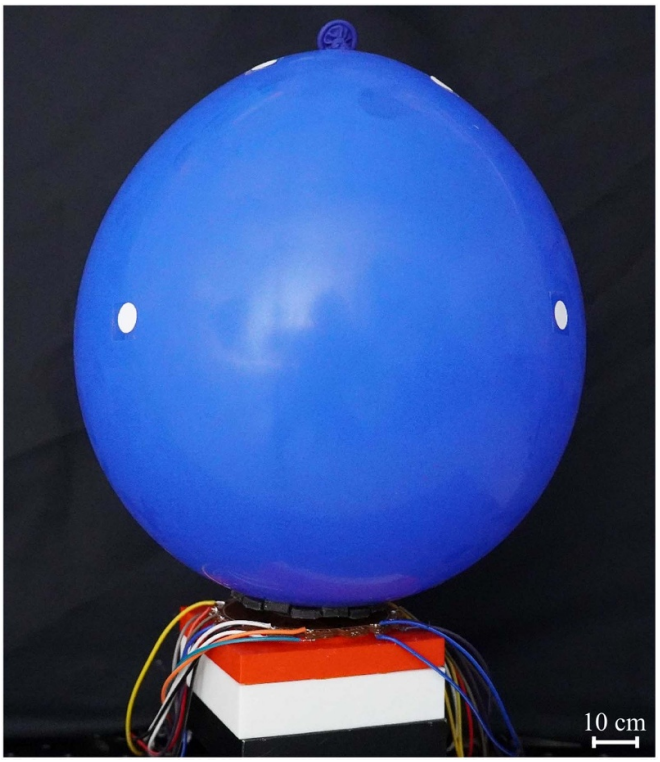

Figure 14. Actuator loaded with a balloon partially filled with rice.

5. Discussion

The work presented in this paper showed the ability of soft magnetic composite materials to create traveling waves, thus leading to rotational actuation. This approach has some limitations as it requires the soft magnetic composite material to be initially curved away from the stiffer electromagnetic coils, yet also close enough to deform according to the magnetic fields. In-plane piezoelectric traveling wave actuators also exist, and soft magnetic composite implementations could be explored in the future. Indeed, in such a design the soft magnetic composite would not move away from the electromagnetic coils but contract and expand in plane [23], thus ensuring optimal exposure to the magnetic fields at all times. Alternatively, curvature in the soft magnetic composite layer could also be created by producing stronger repelling electromagnetic fields, either using asymmetric driving signals or permanent magnets and composites. Piezoelectric traveling wave actuators also usually employ a "tooth-like" contact surface between stator and rotor. Such a structure is as relevant here as it is in traditional actuators and may improve our actuator performance, but would rely on a different manufacturing process when joining the separate soft magnetic composite sections. Future work may also address the flat electromagnetic coil design as an optimized design would permit a reliable efficiency comparison between this design and other soft actuators designs.

6. Conclusion

In this work we generated traveling waves in a soft circular magnetic elastomer structure. We successfully used these waves to spin a balloon and PMMA disks. The use of rigid PMMA rotors allowed us to determine the actuator's torque and rotation velocity using loads of various masses. The actuator attained a maximum average rotation velocity of to 4.9 rpm (m1 = 7.51 g) and a maximum average torque of to 2.6 mN·m (m4 = 17.6 g) (figure 12). The actuator also reached a maximum average mechanical power of 0.8 mW using the 4 mm PMMA plate (m3 = 12.17 g) with an efficiency of about 0.17% (figure 13). Our soft actuator can be used to spin soft objects, as we demonstrated by rotating a 17 g balloon at up to 6.2 rpm (figure 14).

Since our actuator's torque transmission mechanism relies on friction, it does not necessitate an additional rigid transmission mechanism [4, 18, 19]. At equivalent rotation speed, our actuator roughly provides ten times the torque with a diameter four times smaller than the soft DEA actuator presented in [19]. Other presented actuators can feature significantly higher rotation speeds [4, 6, 18], but also rely larger form factor as well as rigid elements.

Our work proposes an innovative way to transmit torques and rotations within soft structures. Core to this work was the idea that continuous rotation in soft structures must adopt friction-based actuation rather than try to mitigate it. This is the first work successfully reporting the generation of traveling waves in a soft bi-directional rotating actuator, as well as the first use of soft magnetic composites to produce the traveling waves.

Data availability statement

The data that support the findings of this study are publicly available: https://doi.org/10.7910/DVN/UYUZKV.

Acknowledgments

This project has received funding from the European Union's Horizon 2020 research and innovation programme under the Marie Skłodowska-Curie Grant Agreement No 101032223. Original high speed camera video files can be found in the repository linked to this article, while the Python code can be found in the following repository: https://github.com/jb-chossat/TravelingWave We sincerely thank Prof. Reis for granting us access to the fleXlab, as well as Dr Abbasi and Dr Yan for helping us with the impulse magnetizer operation. We would also like to also extend our sincere thanks to Dr Leroy for his encouragements and thoughtful comments during this work's genesis.

ORCID iDs

Jean-Baptiste Chossat https://orcid.org/0000-0003-2264-5830
Herbert Shea https://orcid.org/0000-0003-3527-3036

References

[1] Jumet B, Bell M D, Sanchez V and Preston D J 2022 *Adv. Intell. Syst.* **4** 2100163
[2] Hawkes E W, Majidi C and Tolley M T 2021 *Sci. Robot.* **6** eabg6049
[3] Christopher M 2023 International Federation of Robotics *Executive Summary - Industrial Robots (Lyoner Str* vol 18 (VDMA Services GmbH) p 60528
[4] Anderson I A, Hale T, Gisby T, Inamura T, McKay T, O'Brien B, Walbran S and Calius E P 2010 *Appl. Phys.* A **98** 75–83
[5] Rosset S and Shea H 2015 Towards fast, reliable and manufacturable deas: miniaturized motor and rupert the rolling robot *Electroactive Polymer Actuators and Devices (EAPAD) 2015* vol 9430 (SPIE) pp 44–54
[6] Kohls N D, Balak R, Ruddy B P and Mazumdar Y C 2023 *Soft Robot.* **10** 912–22
[7] Lu S M 2016 *Renew. Sustain. Energy Rev.* **59** 1–12
[8] Tian X, Liu Y, Deng J, Wang L and Chen W 2020 *Sens. Actuators* A **306** 111971
[9] Ohm C, Brehmer M and Zentel R 2010 *Adv. Mater.* **22** 3366–87
[10] Jani J M, Leary M, Subic A and Gibson M A 2014 *Mater. Des.* **56** 1078–113
[11] Rousseau I A 2008 *Polym. Eng. Sci.* **48** 2075–89
[12] Baumann A, Sánchez-Ferrer A, Jacomine L, Martinoty P, Le Houerou V, Ziebert F and Kulić I M 2018 *Nat. Mater.* **17** 523–7
[13] Mirfakhrai T, Madden J D and Baughman R H 2007 *Mater. Today* **10** 30–38
[14] Gong X, Yang K, Xie J, Wang Y, Kulkarni P, Hobbs A S and Mazzeo A D 2016 *Adv. Mater.* **28** 7533–8
[15] Yan J, Zhang X, Xu B and Zhao J 2018 *Soft Robot.* **5** 527–40
[16] Salem L, Gat A D and Or Y 2022 *Soft Robot.* **9** 1134–43
[17] Kornbluh R, Pelrine R, Eckerle J and Joseph J 1998 Electrostrictive polymer artificial muscle actuators *Proc. 1998 IEEE Int. Conf. on Robotics and Automation (Cat. No. 98CH36146)* vol 3 (IEEE) pp 2147–54
[18] Anderson I A, Tse T C H, Inamura T, O'Brien B M, McKay T and Gisby T 2011 *Appl. Phys. Lett.* **98** 123704
[19] Minaminosono A, Shigemune H, Okuno Y, Katsumata T, Hosoya N and Maeda S 2019 *Front. Robot. AI* **6** 1
[20] Mohammadi M, Berggren M and Tybrandt K 2023 *Adv. Intell. Syst.* **2200449** 2200449
[21] Mao G, Schiller D, Danninger D, Hailegnaw B, Hartmann F, Stockinger T, Drack M, Arnold N and Kaltenbrunner M 2022 *Nat. Commun.* **13** 4456
[22] Dickey M D, Chiechi R C, Larsen R J, Weiss E A, Weitz D A and Whitesides G M 2008 *Adv. Funct. Mater.* **18** 1097–104
[23] Kim Y, Yuk H, Zhao R, Chester S A and Zhao X 2018 *Nature* **558** 274–9
[24] Zhao R, Kim Y, Chester S A, Sharma P and Zhao X 2019 *J. Mech. Phys. Solids* **124** 244–63
[25] Wang L, Kim Y, Guo C F and Zhao X 2020 *J. Mech. Phys. Solids* **142** 104045
[26] Kim Y and Zhao X 2022 *Chem. Rev.* **122** 1520–6890
[27] Kim Y, Parada G A, Liu S and Zhao X 2019 *Sci. Robot.* **4** eaax7329
[28] Lu H, Zhang M, Yang Y, Huang Q, Fukuda T, Wang Z and Shen Y 2018 *Nat. Commun.* **9** 1–7
[29] Zhang J, Ren Z, Hu W, Soon R H, Yasa I C, Liu Z and Sitti M 2021 *Sci. Robot.* **6** eabf0112
[30] Reiche M, Becker T I, Stepanov G V and Zimmermann K 2023 *Soft Robot.* **10** 770–84 (available at: www.liebertpub.com/doi/full/10.1089/soro.2022.0106)

[31] Uchino K and Giniewicz J R 2003 *Micromechatronics Materials Engineering* (Marcel Dekker)
[32] Flynn A M 1995 Piezoelectric ultrasonic micromotors *PhD Thesis* Massachusetts Institute of Technology Dept. of Electrical Engineering and Computer Science
[33] Uchino K 1998 *Smart Mater. Struct.* **7** 273
[34] Mashimo T and Terashima K 2015 *IEEE/ASME Trans. Mechatronics* **20** 2699–707
[35] Park S, Mondal K, Treadway I I I R M, Kumar V, Ma S, Holbery J D and Dickey M D 2018 *ACS Appl. Mater. Interfaces* **10** 11261–8
[36] Diller E, Zhuang J, Zhan Lum G, Edwards M R and Sitti M 2014 *Appl. Phys. Lett.* **104** 174101
[37] Bastola A K, Paudel M, Li L and Li W 2020 *Smart Mater. Struct.* **29** 123002
[38] Haussener T, Momenzadeh N and von Lockette P 2021 *J. Magn. Magn. Mater.* **539** 168415